In-situ Monitoring of Thin-Wall Build Quality in Laser Powder Bed Fusion using Deep Learning

Aniruddha Gaikwad[1], Farhad Imani[2], Hui Yang[2], Edward Reutzel[3], and Prahalada Rao[1]
[1] Department of Mechanical and Materials Engineering,
University of Nebraska-Lincoln, NE, USA
[2] Harold and Inge Marcus Department of Industrial and Manufacturing Engineering,
Pennsylvania State University, PA, USA.
[3]Applied Research Laboratory, Pennsylvania State University, PA, USA

Abstract

The goal of this work to mitigate flaws in metal parts produced from laser powder bed fusion (LPBF) additive manufacturing (AM) process. As a step towards this goal, the objective of this work is to predict the build quality of a part as it is being printed via deep learning of in-situ layer-wise images obtained from an optical camera instrumented in the LPBF machine. To realize this objective, we designed a set of thin-wall features (fins) from Titanium alloy (Ti-6Al-4V) material with varying length-to-thickness ratio. These thin-wall test parts were printed under three different build orientations and in-situ images of their top surface were acquired during the process. The parts were examined offline using X-ray computed tomography (XCT), and their build quality was quantified in terms of statistical features, such as the thickness and consistency of its edges. Subsequently, a deep learning convolutional neural network (CNN) was trained to predict the XCT-derived statistical quality features using the layer-wise optical images of the thin-wall part as inputs. The statistical correlation between CNN-based predictions and XCT-observed quality measurements exceeds 85%. This work has two outcomes consequential to the sustainability of additive manufacturing: (1) It provides practitioners with a guideline for building thin-wall features with minimal defects, and (2) the high correlation between the offline XCT measurements and in-situ sensor-based quality metrics substantiates the potential for applying deep learning approaches for the real-time prediction of build flaws in LPBF.

Keywords: Additive manufacturing (AM), laser powder bed fusion (LPBF), thin-wall features, in-situ imaging, deep learning, real-time monitoring, design guidelines, quality assurance.

1 Introduction

1.1 Background and Motivation

The goal of this work is to mitigate flaws in metal parts made using laser powder bed fusion (LPBF) additive manufacturing (AM) process through in-situ sensor-based monitoring and diagnosis. In LPBF (Figure 1), a thin layer of powder is raked or rolled across a build plate, and subsequently, this layer of powder is selectively melted using energy supplied by a laser beam [1].

For most materials processed with LPBF, the power of the laser beam is set in the range of 200 W to 500 W, and its scanning velocity ranges from 500 mm/s and 1000 mm/s. After a layer is selectively melted, the build plate is lowered by a distance typically in the range of 50 µm to 100 µm, and another layer is deposited [1, 2]. This process continues until the part is built. In LPBF, the build quality of the part is governed by a complex intertwined relationship between the part geometry, process parameters, material characteristics, and thermal phenomena [1-4].

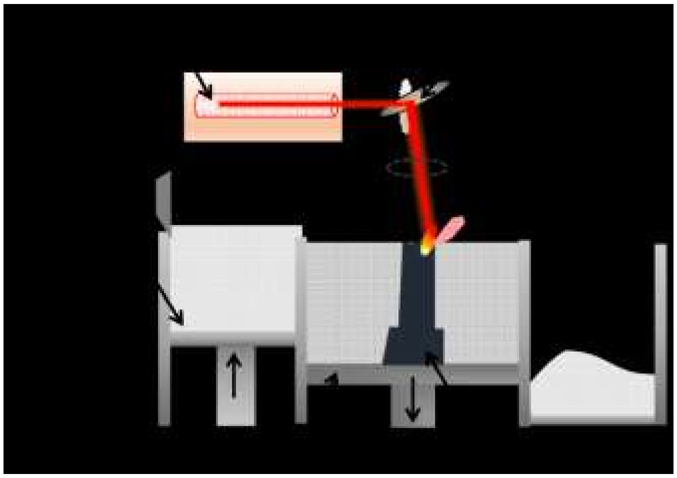

Figure 1: Representation of the laser-based powder fusion process [5].

This work concerns the printing of thin-wall structures using LPBF. Thin-wall structures are extensively used in industrial applications for a variety of reasons, but mainly to reduce the weight of a component without compromising the structural integrity [6]. For example, Figure 2 shows a titanium spinal implant consisting of thin-wall structures. Such intricate geometry is difficult to make with conventional subtractive and formative manufacturing process [7-9].

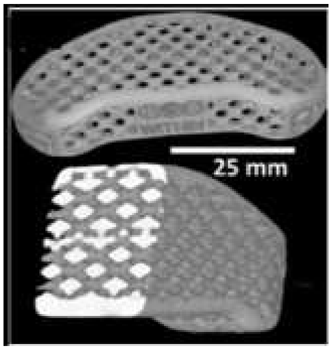

Figure 2: X-Ray computed tomography (XCT) scan of a titanium spinal implant consisting of thin-wall structures [10].

The intricate geometry of thin-wall structures, however, makes them susceptible to a variety of failures during LPBF. The geometric integrity of a thin-wall depends on two key factors:

(1) The process parameters, such as laser power, material properties, and orientation of the part with respect to the recoater blade.

(2) The dimensions of the thin-wall, particularly the thickness in relationship to the length and height of the thin wall. For instance, if the thin-wall is too fragile to resist the lateral force of the recoater, it will collapse. As exemplified in Figure 3 (b), if the thin-wall is overly tall in the vertical build direction, or long with respect to its thickness, it will collapse. These challenges have motivated the need to study the design for additively manufactured thin-wall geometries.

The causal phenomena for failure of the thin-walls is that their small cross-section impedes the flow of heat generated by the laser. The restricted heat flux leads to sharp thermal gradients, which in turn may cause cracking and warping (distortion) defects [11, 12]. Another common reason for the frequent failure of thin-walls is the interaction between thermal and mechanical factors. The geometric distortion of the thin-wall due to thermal gradients causes the part to protrude out of the powder bed, a phenomenon called super-elevation, which leads to part contact with the recoater [13]. The part-recoater contact, apart from damaging the machine, is liable to cause build flaws in the thin-wall, including complete collapse, due to the shear force exerted on the part by the recoater. Despite a priori process optimization, these thermal-induced failures are difficult to predict. In other words, there is a stochastic aspect to thin-wall failures. Given these risks, there is a compelling need to detect imminent build failures in thin-wall LPBF parts using sensor data [14-16].

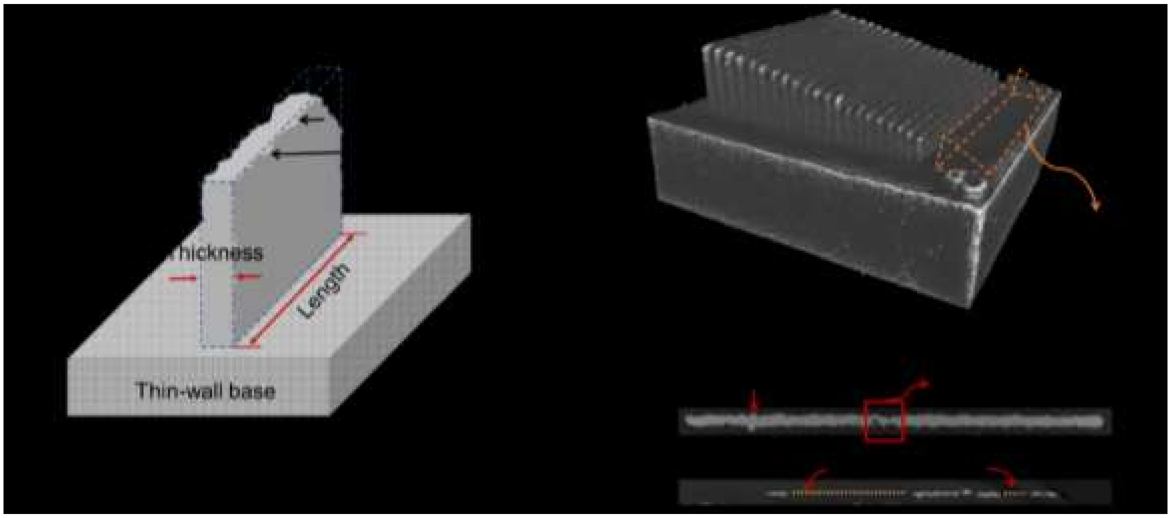

Figure 3: (a) Various defects that may occur in a thin-wall structure built using LPBF process. (b) XCT scan of a thin-wall part at 60° orientation angle. The thin-walls with aspect ratio of 55 (l/t, 11 mm/ 0.15 mm) and 36 (l/t, 11 mm/ 0.1 mm) are shown (c1) and (c2) respectively. These images depict the different defects in thin-wall structures.

1.2 Objective and Approach

The objective of this work is to detect the incipient failure of thin-wall structures through layer-by-layer images of the part obtained using an optical camera instrumented inside an LPBF machine. To address this objective, we develop and apply an artificial intelligence approach called deep learning neural networks. The key idea is to devise a convolutional neural network (CNN) trained to recognize and predict the impending failure of a thin-wall structure from in-situ sensor data.

The approach consists of three tasks. First, we designed experiments to print a test artifact having thin-wall features. The details of test artifact are discussed in Section 3.1 (see Figure 5). Four such test parts were built under varying orientations with respect to the recoater blade direction. We developed an optical imaging setup that takes a picture of the surface of the part after each layer is deposited. Second, once thin-wall structures were printed, we characterized their build quality using offline X-ray computed tomography (XCT); XCT is a non-destructive approach that can capture both the internal and external morphological aspects of a part. The quality of the thin-wall build is quantified through morphological features extracted from layer-wise XCT slices via image processing. These features are used as derived or surrogate metrics of thin-wall build quality.

Third, the layer-wise images (obtained in the first task) are used as inputs to a convolutional neural network (CNN) trained to predict the thin-wall build quality in terms of the surrogate quality features extracted from the XCT analysis (second task). We demonstrate that the CNN tracks the quality of the thin-wall part in terms of its build quality, which in the future will be valuable to preempt build failure.

1.3 Challenges and Novelty

Machine learning techniques, including CNN, are being increasingly applied in the AM domain for detection of flaws; a brief review of recent advances in this area are provided in Section 2. While machine learning approaches are well-known in the literature, and have been applied in various domains ranging from healthcare to manufacturing, the application of machine learning to AM is suffused with the following challenges.

First, conducting extensive parametric studies in AM is an expensive proposition, especially in LPBF, given the cost of the powder (the titanium alloy powder used in this work costs over 200 dollars per pound), slow nature of the process (build time is over 6 hours for the thin-wall part), and cumbersome nature of post-processing and defect characterization. For example, the thin-wall parts built in this work are examined offline using X-ray computed tomography (XCT); it requires several hours to XCT a thin-wall part.

Consequently, in AM the scope to conduct a full-scale design of experiments to obtain training data with different shapes, and varying multiple parameters (there are over 50 variables in LPBF alone) is prohibitive in terms of cost and time. Accordingly, a rich dataset for training and testing a machine learning model across a broad expanse of defects is inherently expensive. Therefore, a major challenge inherent to AM is that the machine learning techniques developed tend to be specific to a particular machine, material, and part shape.

Second, the defects in AM are multi-scaled, i.e. they range from a few micrometers to the macroscopic millimeter scale. For instance, porosity is typically less than 100 µm, while distortion in geometry is in the scale of 1 mm and above. It may not feasible to use one type of sensor data within one type of machine learning model to detect all types of flaws.

Contingent on these challenges, the novel aspect of this work is in detecting flaws in the geometric integrity of thin-wall features through in-situ optical imaging data and deep learning (CNN). The practically relevant outcomes of this work in the AM context are: (1) design guidelines for making thin-wall geometry parts in terms of their length-to-thickness ratio contingent on the orientation, and (2) demonstrate that part defects are predicted using the CNN as a function of in-situ images and validating the predictions through ground-truth XCT characterization.

1.4 Organization of the paper

The rest of this paper is organized as follows. Section 2 presents a brief summary of the literature from the perspective of in-situ sensing and deep learning neural networks in the context of their application to process monitoring in AM. This is followed by the description of experimental design and procedure in Section 3, including experimental build conditions of thin-wall test artifact and the procedure for data acquisition. Section 3 also describes the methodology used for quantification of thin-wall build quality from XCT scan data and key aspects of the CNN. The results from this work are discussed in Section 4, in which the performance of CNN predictions is compared with XCT-quantified thin-wall quality. Finally, the conclusions stemming from this work, and avenues for future research are summarized in Section 5. The detailed description of the deep learning CNN used in this work is given in Appendix II.

2 Literature Review

Process repeatability and part consistency remain compelling challenges in AM. Accordingly, there is active research interest directed at in-situ sensor-based monitoring, online analytics, and process control [14, 15, 17-19]. The thrust is in isolating the type, location, and severity of flaws with in-situ sensors, and subsequently, implementing a process control system designed to correct these flaws inside the machine [20]. A variety of sensors, including infrared thermography, optical spectroscopy, pyrometry, among others, are reported in the literature for in-situ flaw identification and estimation. Given the vast scope of this area, we restrict our review to the pioneering developments that combine optical imaging and machine learning for flaw detection in LPBF.

Similar to the approach discussed in our work, Nassar *et al.* devised an in-situ sensing and monitoring technique, wherein they used a supervised machine learning approach to detect defects from in-situ optical images [21]. The authors proposed a methodology to predict defects, such as cracks, porosity, incomplete fusion, by first identifying these flaws from the X-ray computed tomography (XCT) scan of the test specimen. These flaws were then mapped onto the layer-wise optical images. Subsequently, a support vector machine model was used to isolate the location of flaws in the optical image with an accuracy of over 80%.

Abdelrahman *et al.*, in a recent work, developed an in-situ flaw detection system with layer-wise optical imaging of a powder bed fusion process [22]. This system captured images of the powder bed prior to and post re-coat of the layer, and each of these images were captured in five different lighting schemes to magnify the surface perturbations, resulting in high defect detection accuracy. The test specimen had intentional built-in defects, and these defects were detected by correlating the multiple lighting condition images across neighboring layers. This approach achieved a specificity 0.84 and sensitivity of 0.915.

Further, recent works by Scime and Beuth demonstrate the application of machine learning for in-situ monitoring of LPBF [23, 24]. The authors used an optical camera to acquire layer-by-layer powder bed images of the EOS M290 LPBF machine. A computer-vision and machine learning algorithm was developed to monitor flaws, such as recoater hopping, recoater streaking, debris formation, super-elevation, part failure and incomplete spreading of powder [23]. A widely used machine learning algorithm called bag-of-words (BoW) was employed to classify various flaws with an accuracy from 65% to 99%. In addition, the authors tested the algorithm by analyzing the efficacy of various support structure schemes. The algorithm was satisfactorily able to detect flaws during the build process. In their latest work, Scime and Beuth developed a CNN to detect and classify the process flaws using optical powder bed images as inputs [24]. The novel multi-scale CNN (MsCNN) resulted in better flexibility and classification accuracy while mitigating many human labeling-related biases. The classification accuracy of the MsCNN was compared with the previously used BoW ML algorithm and a conventional CNN. The MsCNN was reported to have the best performance in comparison to the other two methods. For instance, the lowest classification accuracy of a process condition in case of MsCNN was 72.7%, and that of BoW and conventional CNN was 39.5% and 0.0% respectively.

Yuan *et al.* used a CNN to monitor the quality of single tracks (lines) of LPBF sintered material deposited under varying conditions of laser power and laser scanning velocity [25]. Images from a co-axial high-speed video camera are used as inputs to the CNN, which is trained from pre-labeled offline characterization data to predict the consistency of the deposited track in terms of the mean and standard deviation of the track width. The R^2 values of 0.93 and 0.70 were achieved for predicting mean and standard deviation of single tracks, respectively.

Imani *et al.* demonstrate the use of in-situ optical imaging techniques to predict the underlying process condition in a machine learning framework [5]. Simple cylindrical test parts were created under varying conditions of laser power, laser scanning velocity, and hatch spacing. The XCT images of these test parts were analyzed, and the effect of process conditions on the distribution, size, and frequency of lack-of-fusion related pores were quantified. In parallel, in-situ images of the part were analyzed using spectral graph theory and multifractal quantification approaches. The features extracted from these analyses were used as inputs within a variety of machine learning algorithms trained to identify the particular process conditions under which the parts were produced.

Williams *et al.* recently implemented deep learning to detect defects, such as porosity and surface imperfections in titanium alloy and nickel alloy samples [26]. To do this, they developed a deep learning CNN termed as Densely-connected Convolutional Block Architecture for Multimodal Image Regression (DCB-MIR). This neural network takes spatially resolved acoustic spectroscopy derived acoustic velocity maps to generate an optical micrograph. The authors propose that the cosine similarity between the optical signatures and the optical micrograph images derived from the DCB-MIR ranges from 0.25 to 0.60.

Aminzadeh developed an in-situ quality inspection setup for LPBF [27]. In this research, Aminzadeh used a high resolution visible-light camera imaging setup to inspect the cross-sectional geometry and porosity in a part. Image processing algorithms were developed to extract information, such as location, shape and size of defects along with detecting porosity in the layer-wise camera images. A qualitative assessment of the pores was done by implementing a statistical Bayesian framework, which is trained with select features that are extracted from the sub-regions of the layer-wise images. It is reported that the Bayesian network performs with precision of 89% and negative predictive value of 83%. This machine-vision system coupled with the analytical framework provides a foundation for systems with alternative sensors, such as height mapping sensors and stereo imaging.

Clijsters *et al.* propose a heterogeneous sensing system along with a novel data analysis technique to monitor part quality in LPBF [28]. The sensing system comprises of a near-infrared thermal CMOS camera and a photodiode. The data from the thermal camera was used to extract information regarding the meltpool, such as area, length and width. Similarly, the photodiode signal was adopted to record the intensity of the meltpool. A mapping algorithm was devised to incorporate meltpool data gathered from both sensors. The maps were then used to monitor phenomena, such as overheating of meltpool, detection of pore position in 2 (X-Y plane) and 3 dimensions. The authors validated the effectiveness of their sensing setup and data analysis algorithm on parts made of Ti6Al4V and AlSi10Mg.

Chen *et al*. recently published a study on the effect of design parameters, such as recoating orientation, hatching pattern, width and height on the edge roughness of thin-wall structures [29]. The authors propose a novel way of characterizing the edge roughness of a thin-wall by registering the XCT images of the build to the CAD model. Further, they perform an analysis of variance study to determine the effect of each design parameter on the thin-wall edge roughness. They also report a predictive model that quantifies the behavior of edge roughness as a function of design parameters. The model suggests that hatching pattern, width and recoater orientation have significant impact on edge roughness of thin-walls.

Similar to our work, Imani *et al.* advanced an in-situ layer-wise monitoring methodology for LPBF that applies computer vision and machine learning algorithms [30]. The authors use the CAD model of the part to register and segregate the region-of-interests (ROIs) in every layer-wise optical image. Next, they propose a novel dyadic partitioning method to distribute each ROI into equal size and in multiple scales. The spatial characteristics of each sub-region ROI is modeled with the help of a semiparametric spatial model. Further, these spatial characteristics are used as inputs to a deep neural network (DNN) which recognizes defects in in-situ optical images. The authors report that the DNN has specificity of 93.85%, positive predictive value of 90.01%, and accuracy of 92.05%.

This paper has the following aspects that are different from these previous works that use deep learning. First, this work is concerned with the detection of build failures in a part having a distinctive and functional feature, namely thin-wall structures, as opposed to characteristics of a single-track or process-centric failures such as recoater hopping. Second, functionally critical build quality characteristics, such as the thickness and consistency of multi-layer thin-walls are observed and quantified from layer-wise XCT analysis, as opposed to visual or optical demarcation. XCT analysis provides a non-destructive means to characterize both the internal and external aspects of the part which is not possible using any other approach. Thirdly, the XCT-derived build quality metric is predicted through a convolutional neural network using in-situ optical images. This layer-wise monitoring of the part build quality will provide the user with in-depth information of the part condition as opposed to a binary classification, such as in-control or out-of-control.

In closing this section, for a physical perspective on finding the optimal build and process parameters for LPBF of thin-walls we point the reader to the works of Thomas [31], Kranz *et al.* [32], and Dunbar *et al.* [33]. Daniel Thomas conducted a detailed study on design rules for AM for his doctoral dissertation [31]. Among many parts, he studied the thin-wall geometry, and reported that to obtain good part quality for a thin-wall, it is necessary to build them at a minimum thickness of 0.4 mm. A similar study done by Kranz *et al.* on thin-wall geometry concludes that a minimum thickness of 0.4 mm must be adhered to [32]. Further, a recent study was done by Dunbar *et al.* on the effect of thin-wall orientation angle with respect to both the build platform (X-Z plane) and also the recoater blade direction (X-Y plane) on porosity within the thin-wall.

It was concluded that to obtain thin-walls with consistent thickness the orientation angle with respect to the build platform should be 90°, and the orientation angle with respect to the recoater blade direction should be 45° [33]. The key points of difference in Dunbar *et al.*'s work with our own are as follows.

(i) In Dunbar *et al.*'s work the thin-walls are individual, free-standing features, and not constituent features of a part as in our test artifact shown in Figure 3. Consequently, the space between each of the thin-walls is of the order of several millimeters, which can substantially reduce resistance to the flow of powder. Moreover, because the thin-walls are largely independent of each other, the collapse (build failure) of one thin-wall has little impact on the rest.

(ii) More importantly, Dunbar *et al.* have not tested the build orientation equivalent to 90° angle with respect to the recoater blade, and they held the aspect ratio constant (9.65 mm × 1 mm × 63.5 mm, length × thickness × nominal vertical height). We note that in Dunbar *et al.*'s convention, their 0° build orientation angle is equivalent to the 90° orientation angle in our work, and vice versa.

(iii) Dunbar *et al.* varied the laser power, velocity, and scan type with the intent of minimizing internal inconsistencies (porosity) and median thickness [33]. While in our work the orientation angle and aspect ratio (length to thickness ratio) is varied, with other processing parameters, such as laser power and laser scan speed, are fixed at manufacturer recommended settings. Moreover, we assess both the internal and geometry-related flaws, including consistency of thickness, porosity and variation in boundary of a thin-wall.

Despite these differences, there is a consistent observation in our work and that of Dunbar *et al.,* that thin-walls sintered with the long edge parallel to the recoater direction (termed 0° orientation angle in our work, 90° orientation angle in Dunbar *et. al.*'s work) have consistent thickness and internal structure compared to other tested combinations. The literature thus substantiates that the surface morphology of a thin-wall is greatly affected by the orientation angle it is built at with respect to the recoater direction.

3 Research Methodology

This section is stratified into two sub-sections. Section 3.1 describes the experimental procedure, including design and processing conditions of thin-wall test parts, and the in-situ sensing approach. In Section 3.2, we detail the approach used to predict the thin-wall quality. From a broad perspective, the approach has two aspects as schematically reported in Figure 4. The first aspect concerns the offline quantification of the thin-wall part quality. For this purpose, the XCT image from a layer of the part is matched (image registration) to its intended CAD design, which allows comparison of the quality of the obtained thin-wall part to its ideal (flaw-free) state. The layer-by-layer deviation of as-built thin-wall from its intended CAD model is quantified in terms of four statistical features. These statistical features are devised to capture critical quality-related aspects of the thin-wall such as its width (thickness), consistency of its edges, presence of internal flaws, and structural integrity. Subsequently, these four statistical features are consolidated into a single, global quantity called the Mahalanobis-squared distance that substitutes as a representative surrogate measure of thin-wall quality.

The second aspect of the methodology relates to the online prediction of the thin-wall part quality. In this part of the methodology, a CNN is trained to predict the XCT-derived Mahalanobis-squared distance given in-situ layer-wise images of the part (on the top surface of the powder bed) acquired from an optical camera. The architecture and details of the CNN used in this work are described in detail in Appendix II.

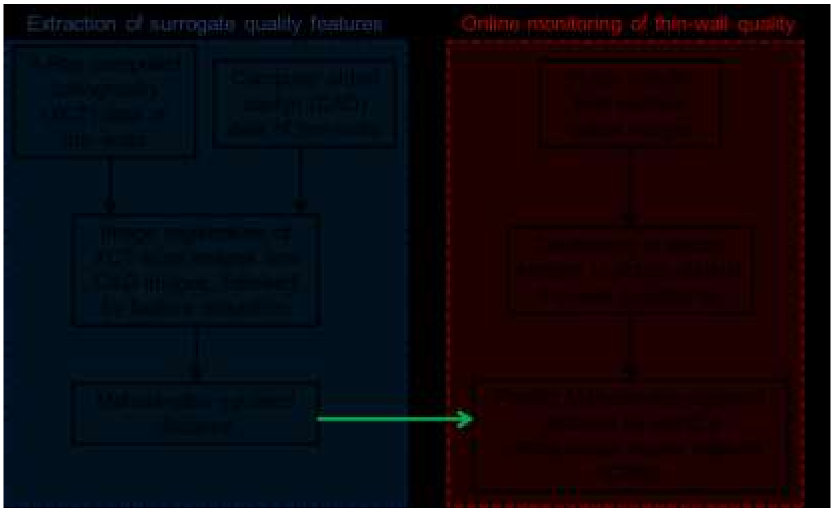

Figure 4: Outline of the methodology proposed to predict the thin-wall quality through XCT analysis and CNN modeling.

3.1 Experimental Studies and Data Acquisition

Titanium alloy (Ti-6Al-4V) parts with thin-wall features exemplified in Figure 5 were built on an EOS M280 LPBF machine. The overall dimensions of the test part are 15 mm × 15 mm × 5.5 mm. Each part includes 25 thin-wall features with a constant length of 11 mm, thickness ranging from 0.06 mm to 0.3 mm in uniform increments of 0.01 mm, while the corresponding height increasing from 0.6 mm to 3 mm in steps of 0.1 mm. The parts are built vertically upwards with 60 μm layer thickness.

The entire part is built in 125 layers. Furthermore, four such thin-wall test parts were built, each at an angular orientation (θ) of 0°, 30°, 60°, and 90° to the direction of the recoater blade in the X-Y plane. The thin-walls built at 30° orientation angle were not analyzed in this work due to lack of XCT data. Referring to Figure 5(d), the aspect ratio of the thin-wall is defined as the length (*l*, largest dimension) to the thickness (*t*, smallest dimension) of the thin-wall; the aspect ratio (*l/t*)of the thin-walls ranges from 36 to 183.

Default parameters recommended by the machine tool manufacturer (EOS M280) were used for building the thin-wall test parts. The following process parameters were used: laser power, P = 340 W; layer thickness, T= 60 μm; hatch spacing, H= 0.12 mm; and laser velocity, V = 1250 mm/s. The test parts (Figure 5) were made using spherical ASTM B348 Grade 23 Ti-6Al-4V powder with a size distribution of 14 μm – 45 μm from LPW Technology, Inc. [10]. The average powder size affects the part quality in LPBF. If the average powder size is exceedingly small, it may lead to porosity due to improper spreading, in contrast, if the average powder size is high it may lead to lack-of-fusion type of porosity, as the laser power may be inadequate to completely melt the powder.

Subsequently, we examine each thin-wall build using X-ray computed tomography (XCT, General Electric V|Tome|X system). The voxel size of the XCT measurement is 15 μm^3. Keeping with the Nyquist sampling criterion, a fault should typically occupy at least two to three voxels of the XCT to be detected. In this work, the faults of interest are at the part-scale, which tend to be in the millimeter range, hence the XCT resolution is adequate. For instance, build flaws, such as discontinuities and inconsistencies in two thin-walls, are evident in the XCT slices in Figure 5(c1 and c2). The layer-wise images of the part on the powder bed are captured using a digital single-lens reflex camera (DSLR, Nikon D800E) with an effective resolution of 36.3 megapixels which is mounted in a custom made enclosure inside the machine [22].

The focal plane is the surface of the build platform. The position of the camera and focus were adjusted heuristically to obtain a sharp image of the powder bed. A representative schematic of the camera, including positioning mounts and sample data acquired from the apparatus is shown in Figure 6. In this work, the distance from the camera focal plane to the center of the powder bed is measured to be approximately 14.5 inch (≈ 368.5 mm).

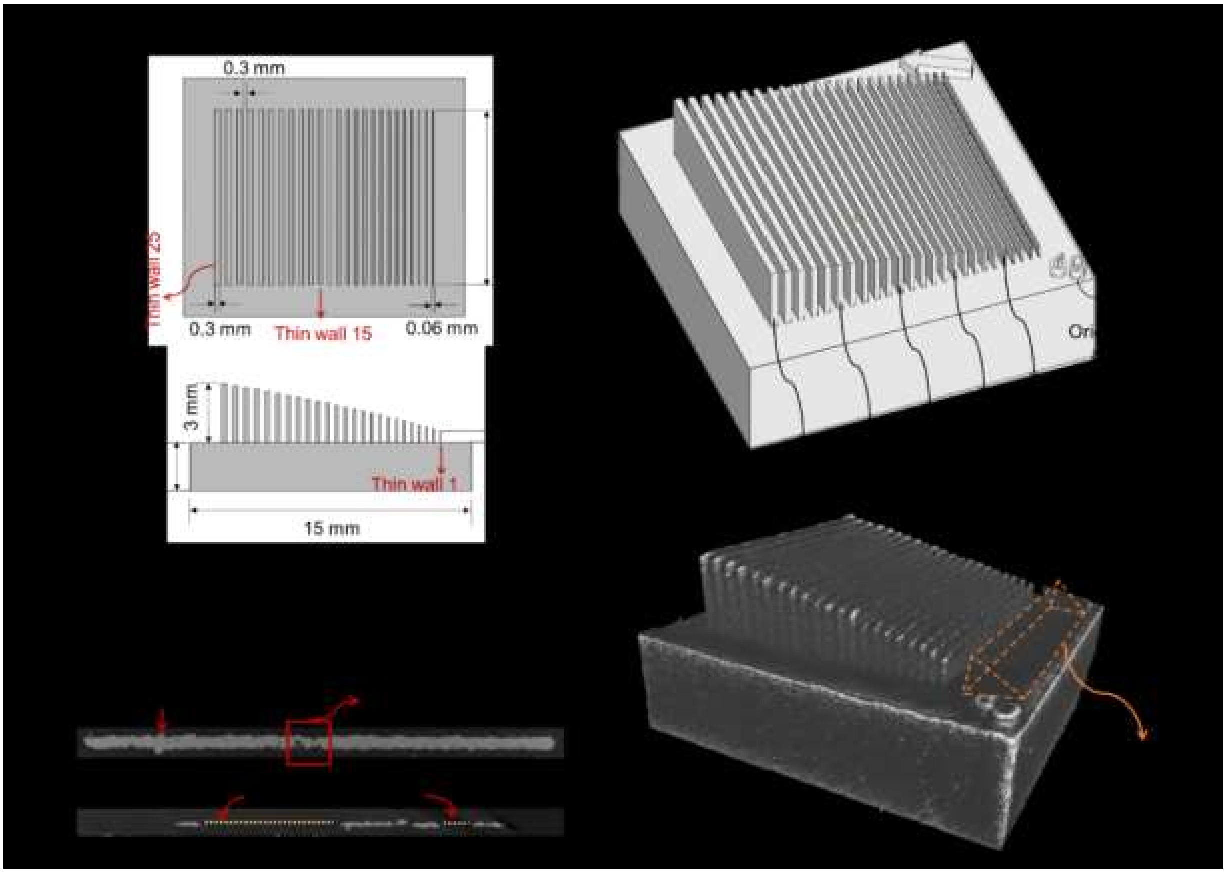

Figure 5: Computer-aided design (CAD) of thin-walls in the test part. (a) Top view, (b) front view. The XCT of the top-view of the thin-walls with an aspect ratio of 73.3 (l/t, 11 mm/0.15 mm) and 36 (l/t, 11 mm/ 0.1 mm) are shown in (c1) and (c2) respectively. These images depict the different defects in thin-wall structures. (d) 3-D CAD view of the test part at an orientation angle of 60° to the recoater blade direction. (e) 3D view of the XCT scan of a thin-wall part at 60° orientation angle [10].

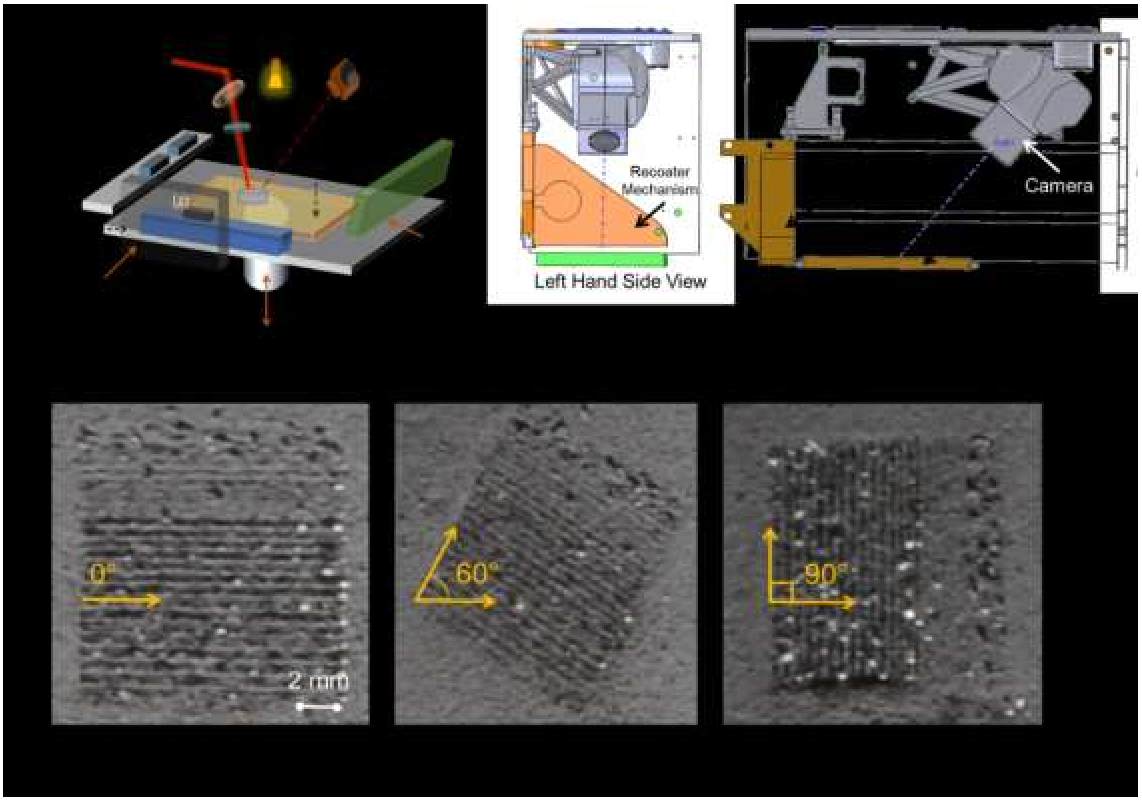

Figure 6: (a) Schematic representation of the in-situ monitoring LPBF setup used in this work. Optical images of a layer of thin-walls being manufactured at different orientation angles in the X-Y plane with respect to the recoater blade direction, namely, (b) 0°, (c) 60°, (d) 90° [10].

3.2 Quantifying the thin-wall build quality using layer-wise XCT scan images

This section describes the analysis of the XCT scan images of the thin-wall geometry. First, the XCT scan of each test artifact is visually (qualitatively) examined layer-by-layer. Figure 7 shows an example XCT image from three thin-wall parts for layer number 18 (1.08 mm build height). Severe damage to the first four thin-walls is evident from XCT image. Also, shown in Figure 7 are zoomed in XCT images for a thin-wall with aspect ratio $l/t = 44$ having thickness $t = 0.25$ mm. This XCT slice provides an insight into the effect of angular orientation on the part quality; at a 90° orientation angle this thin-wall has several structural flaws compared to the 0° orientation.

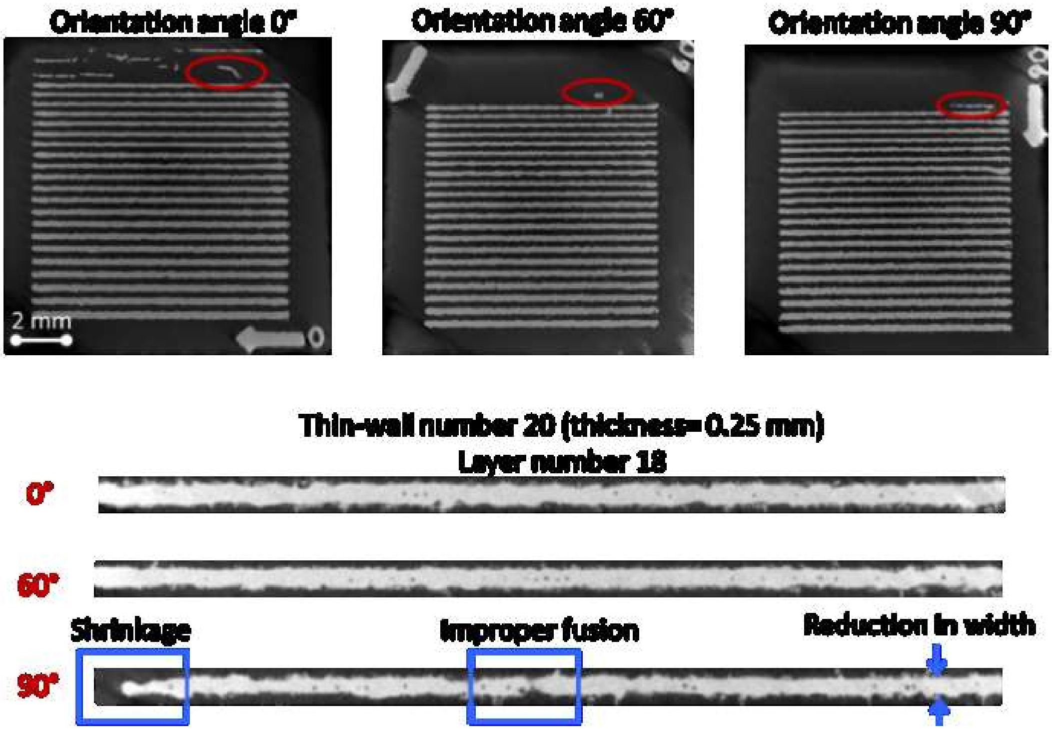

Figure 7: The thin-wall part from three different orientations. The top panel shows the part at layer number 18, and the bottom panel shows the individual thin-wall number 20 (l/t= 44, thickness= 0.25 mm). The 90° orientation angle has the worst build quality [10].

Next, the XCT scan for each thin-wall part is sliced with a layer thickness of 10 µm, resulting in 300 images for each part. The CAD file for each test part is also sliced with an identical resolution of 10 µm. Subsequently, an intensity-based image registration approach is used to perform the affine transformation and align the XCT scan image to the corresponding CAD slice. Finally, individual thin-walls are analyzed from the registered images, as depicted in Figure 8, and the following four quantitative features are extracted (Figure 9). The approach to obtain these quantifiers is described in detail in Ref. [10].

- *Thickness* ($\bar{t}$)*:* This feature quantifies the average thickness of a thin-wall (Figure 9 (a1)) across its length.

- *Density* (ρ_t)*:* Quantifies un-melted or areas devoid of sufficient material that result in pores-like flaws in an individual thin-wall (Figure 9 (b)(right)).
- *Edge smoothness (*σ_s*):* The degree of smoothness or consistency of the thin-wall edge (Figure 9 (b)(left)).
- *Discontinuity (*δ*):* The degree to which there are large non-contiguous gaps in the thin wall Figure 9 (b).

The advantage of these quantifiers is that they are based on two-dimensional image-based measurements, and involve simple matrix algebra, thus significantly reducing the computational burden involved for feature extraction.

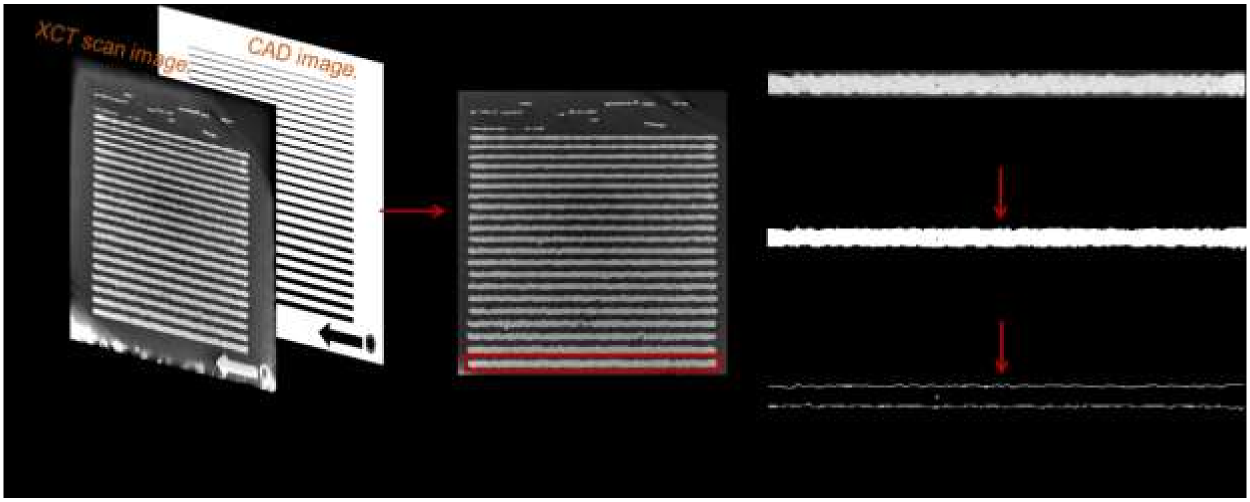

Figure 8:The procedure used extraction of thin-walls from XCT scan images. The thin-wall highlighted in (b) is extracted to as shown in (c). The thin-wall images shown in (d) and (e) are used for feature extraction [10].

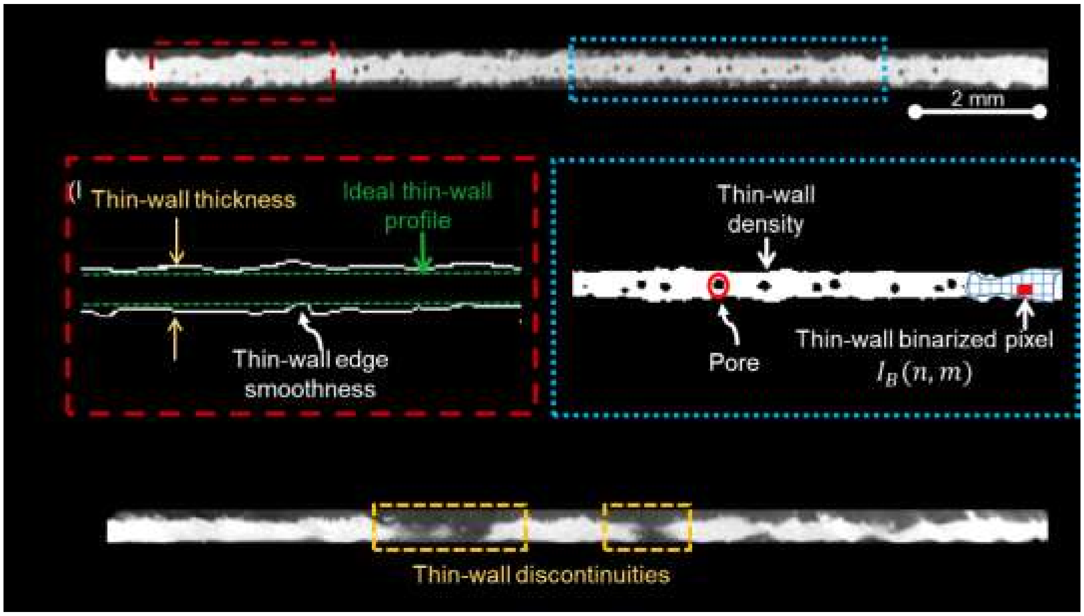

Figure 9: Thin-wall features extracted from XCT scan images. (a) Thin-wall extracted using methodology shown in Figure 8, and (b) shows the three features extracted from the thin-walls, namely, thin-wall thickness, thin-wall edge smoothness, and thin-wall density. (c) Depicts the discontinuity in a thin-wall, which is used as the fourth feature [10].

To obtain a generalized measure of thin-wall quality, the above four quantifiers for each thin-wall are arrayed in a matrix called the *quantifier matrix* (X^{θ}), for each orientation angle θ = {0°, 60°, 90°} as shown in Eqn. (1). Each row in the matrix X^{θ} is representative of a thin-wall, and each column is the representative quality feature.

$$\begin{pmatrix} \overline{t_1} & \sigma_{s1} & \rho_{t1} & \delta_1 \\ \overline{t_2} & \sigma_{s2} & \rho_{t2} & \delta_2 \\ \vdots & \vdots & \vdots & \vdots \\ \overline{t_N} & \sigma_{sN} & \rho_{tN} & \delta_N \end{pmatrix} \tag{1}$$

Next, the quantifier matrix X^{θ} is compared with features extracted from the CAD images of the thin-walls. The features extracted from the CAD slices are considered to be ideal, and hence, the features extracted from the as-built XCT images are compared with the CAD slice.

The metric used for this comparison is known as the Mahalanobis-squared distance ($(D_M^2)_i^\theta$) for orientation angle θ and thin-wall number i = {1, 2, 3…,25} as shown in Eqn. (2).

$$
\begin{gathered}
(D_M^2)_i^\theta = (\bar{X}_i^\theta \ - \mu^{TW})' S^{-1} (\bar{X}_i^\theta \ - \mu^{TW}) \\
\bar{X}_i^\theta = [\overline{t_i} \ \ \sigma_{Si} \ \ \rho_{ti} \ \ \delta_i] \\
\mu^{TW} = [\overline{t_{CAD}} \ \ \sigma_{S(CAD)} \ \ \rho_{tCAD} \ \ \delta_{CAD}].
\end{gathered}
\tag{2}
$$

Where $\bar{X}_i^\theta$ is the feature vector of a particular thin-wall image i for orientation angle θ which is to be compared with the thin-wall features extracted from a CAD image of the thin-wall (μ^{TW}). The features extracted from the CAD image are stored in μ^{TW}, and S^{-1} is the inverse of the variance-covariance matrix derived from the feature matrix of XCT scan images of a thin-wall with a particular orientation angle.

Next, we train a CNN to predict the Mahalanobis-squared distance as a function of the in-situ images of the part. For training the CNN, the input used is an individual thin-wall extracted from layer-wise powder bed images after de-noising, and the output is the corresponding Mahalanobis-squared distance of the thin-wall obtained from the XCT scan image analysis. The data is allocated in the following manner: 80% for training the network, and 20% for testing the network. The data are augmented to create sufficiently dense training and testing data sets. For example, 50 images are available for thin-wall 25, which are augmented to 100 images by changing image contrast and sharpness. Further, 80 images are used to train the CNN and 20 images are used for the testing. The data are randomly selected for training the network, and then the remaining data are used to test the network. The details of the CNN used in this work are provided in the Appendix II.

4 Results

4.1 Observations of thin-wall build quality from layer-wise XCT scan images

We derive the following inferences from the visual observation of the XCT data. This leads to an understanding of the effect of orientation and aspect ratio on the build quality of thin-wall structures. To avoid build flaws, it is best not to present the broadside of the thin-wall to the recoater. This observation is exemplified in Figure 10. Shown in Figure 10(a), are the XCT images for the thin-wall number 10 which has a relative large aspect ratio l/t= 73 (length= 11 mm, thickness t = 0.15 mm) at three different layers. Likewise, Figure 10(b) shows these results for thin-wall number 20 with aspect ratio l/t= 44 (length= 11 mm, thickness t = 0.25 mm). On visual examination of XCT images of Figure 10(a) and (b), it is evident that the maximum height to which the thin-wall can be built is a function of its thickness and orientation.

For example, in the case of thin-wall number 10 with the larger aspect ratio $l/t = 73$, severe build flaws appear at layer 22 and beyond. By contrast, for thin-wall number 25 with much smaller aspect ratio $l/t = 44$ flaws begin to appear close to layer number 35. Further, we observe that irrespective of the aspect ratio the parts printed at the orientation angle (θ) of 90° exhibit poor quality as compared to those printed at 0° and 60° orientation angles. In other words, when the long edge of thin-wall is parallel to the direction in which the recoater moves, the thin-wall feature tends to build with fewer flaws, compared to those thin-wall structures that are built with the broadside of the thin-wall exposed to the recoater. This is because the thin-wall built parallel to the recoater motion offers less resistance to the flow of the powder than that at 90° orientation angle. We conducted a detailed analysis of all thin-walls, and arrive at the following generalized observations,

(1) Thin-walls with thickness less than 0.1 mm (*l/t*= 110) fail to build irrespective of their orientation. The cause of this failure appears to be the overly thin cross-section of the high aspect ratio thin-walls, which is too weak to resist the lateral force exerted by the recoater.

(2) To quantify the foregoing observation, we calculated the Mahalanobis-squared distance for each thin wall per Eqn. (2). An important observation, also evident from Figure 10 (a) and (b), is that beyond a threshold value of 15 for the Mahalanobis-squared distance, the thin-wall quality is typically poor. The threshold value of 15 for the Mahalanobis-square distance seems to be generally applicable to all the combinations of thin-wall aspect ratio and orientation. Accordingly, the Mahalanobis-squared distance is akin to a surrogate measure of thin-wall build quality.

We have summarized the foregoing two observations in terms of Figure 11, which maps the build height versus the aspect ratio averaged across all orientation angles, and recommended build height to achieve good geometrical integrity. The error bar in Figure 11 (a) represents ± 1 standard deviation seen across all orientation angles for a given aspect ratio. Figure 11 (b) depicts this information in greater detail with the recommended height to build thin-walls with good geometrical integrity, and the height at which a thin-walls collapse with respect to a given orientation and aspect ratio.

Our conclusion to build thin-walls at 0° orientation angle with respect to the recoater blade direction are similar to the findings of Dunbar et al. in their recent work [REF]. They observe that thin-walls built at 0° orientation angle and EOS standard parameters are thicker than the ones built at 45° orientation angle and modified parameters (laser power= 100 W and laser scan speed= 900 mm/s). On the contrary, they observe that thin-walls built at 45° orientation angle and modified parameters have low porosity. This conclusion is not surprising as porosity is a function of energy density, i.e., laser power and laser scan speed, and not the orientation angle with respect to the recoater blade.

In this work, we define the thin-wall quality based on its surface morphology and porosity. The orientation angle with respect to recoater direction has a greater effect on the surface morphology. This is because larger the surface area exposed to the lateral force exerted by the recoater blade, poorer will be the surface morphology. Therefore, we suggest that 0° orientation angle should be used to obtain good thin-wall quality.

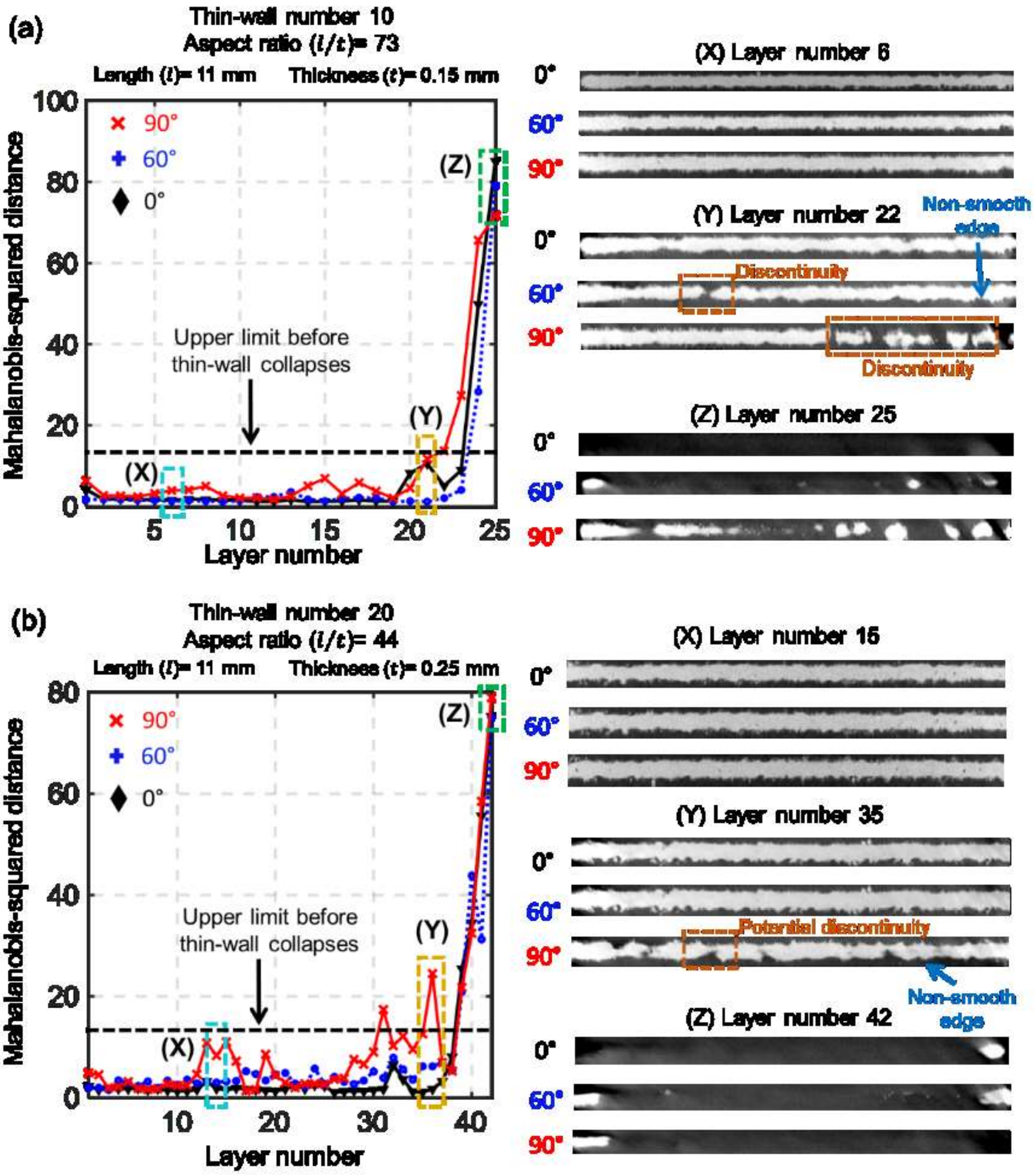

Figure 10: Mahalanobis-squared distance for different orientations (θ) of different thin-walls.(a) Thin-wall number 10, with aspect ratio (l/t) of 73, i.e., length l= 11 mm and thickness t= 0.15 mm. (b) Thin-wall number 20, with aspect ratio (l/t) of 44, i.e., length l= 11 mm and thickness t= 0.25 mm.

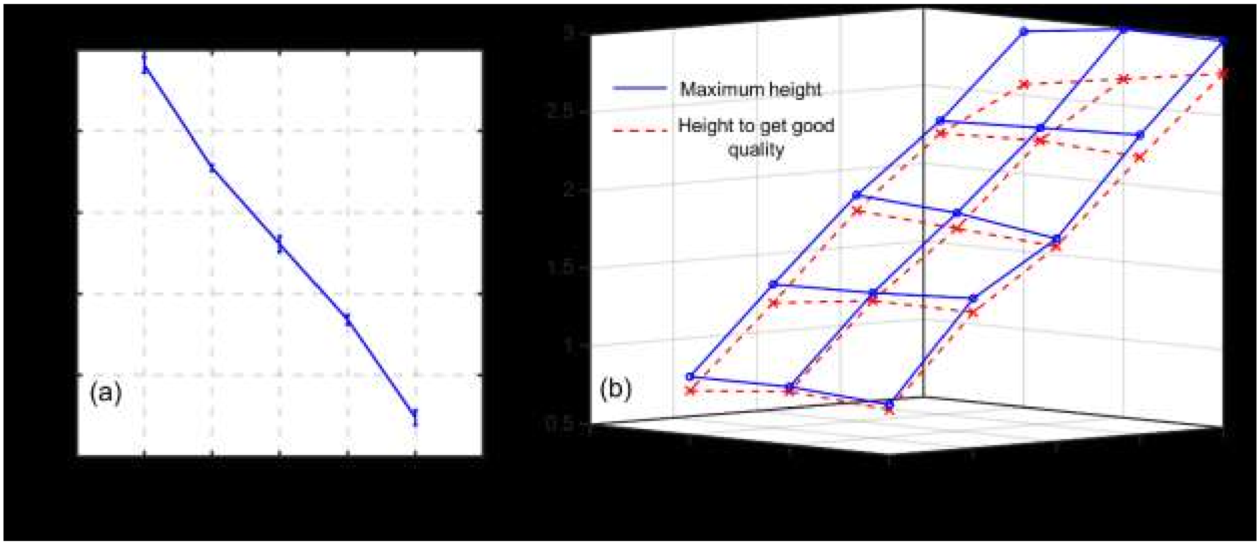

Figure 11: (a) Maximum recommended height to build thin-walls of good geometrical integrity with respect to aspect ratio (l/t). The error bars are ± 1 standard deviation (b) Maximum build height of thin-walls to get good geometrical integrity, and height at which thin-walls collapse, with respect to aspect ratio (l/t) and orientation angle (θ).

4.2 Detecting build failures in thin-wall quality by analyzing in-situ images with CNN

Continuing with our analysis, instead of the XCT to ascertain the thin-wall quality after it is built, we now use the in-situ layer-wise images of the thin-wall as an input to the CNN to predict the build quality. The output (prediction) is the Mahalanobis-squared distance, which h we substantiated from the XCT analysis in Section 4.1 to be a surrogate or derived measure of build quality. Figure 12 depicts the representative results for thin-wall numbers 23 (aspect ratios *l/t* = 39) under the three different angular orientations; the XCT observations are shown as solid lines and CNN-derived predictions are overlain in dotted lines in Figure 12.

Results from Figure 12 indicate that the CNN-derived Mahalanobis-squared distance results closely track those calculated using XCT image analysis of the thin-wall. We recall that a Mahalanobis-squared distance over a threshold 15 is indicative of an onset of build failure. In

Figure 12, when the XCT-derived Mahalanobis number exceeds the value of 15, the CNN also follows suit. Representative XCT images for selected layers are inset in Figure 12 as a ground-truth. The XCT images affirm that the CNN indeed predicts the deterioration in thin-wall build quality.

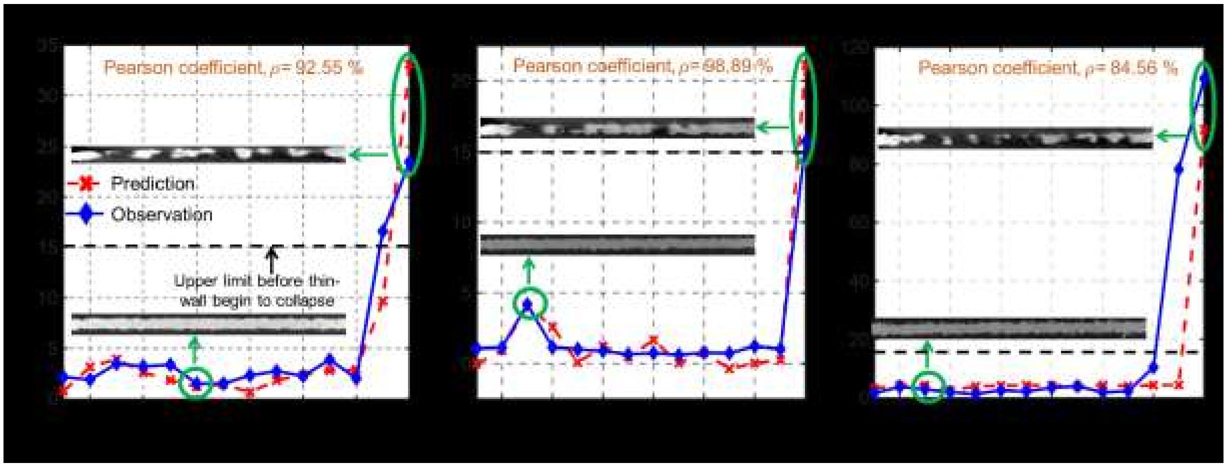

Figure 12: Mahalanobis-squared distance predicted using CNN regression (dotted lines) compared with XCT-derived Mahalanobis-squared distance (solid lines) for thin-wall number 23 (l/t= 39, length= 11 mm, thickness= 0.28 mm) with (a) orientation angle θ= 0°, (b) orientation angle θ= 60°, and (c) orientation angle θ= 90°.

As a quantitative measure to ascertain the closeness between the observed and CNN-predicted Mahalanobis-squared distance trends, we used the Pearson coefficient. For trends shown in Figure 12, the Pearson correlation coefficient ranges from close to 85% to 98%. We further substantiate these results for thin-wall number 25 in Figure 13 with Pearson correlation coefficient ranging from 85% to 96%. The results in Figure 12 and Figure 13 demonstrates that instead of expensive post-process XCT scan measurements, the in-process image data through CNN-based analysis can be used for detecting process defects in LPBF. This work thus paves the way for in-situ real-time monitoring of part quality in AM using optical imaging data

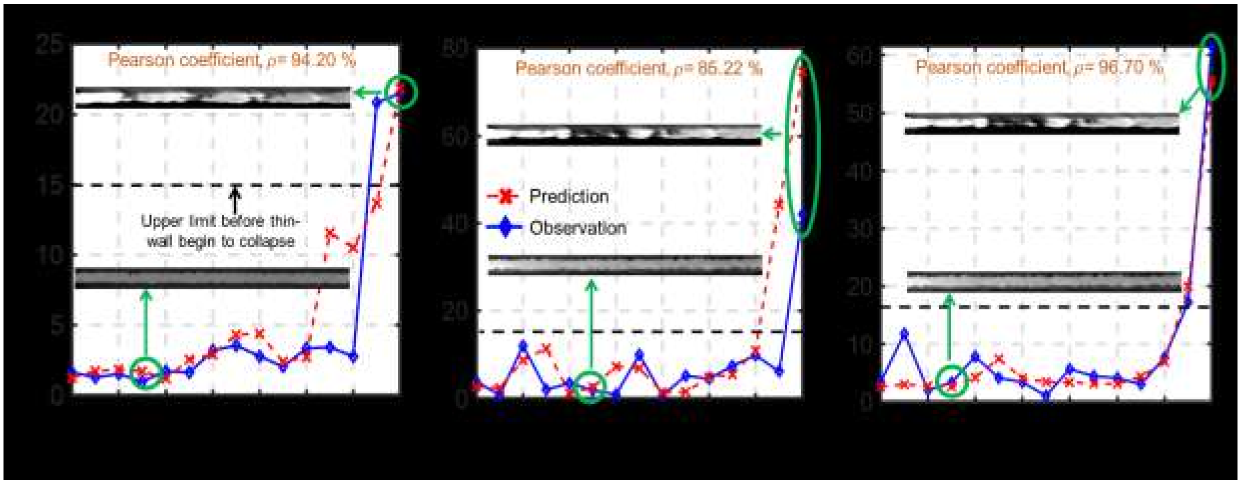

Figure 13: Mahalanobis-squared distance prediction via CNN regression (dotted lines) for thin-wall number 25 (l/t= 36, length= 11 mm, thickness= 0.30 mm) with (a) orientation angle θ= 0°, (b) orientation angle θ= 60° and (c) orientation angle θ= 90°.

5 Conclusions and future work

This work demonstrated the viability of deep learning neural networks to predict incipient build flaws in thin-wall parts made from the LPBF AM process from in-situ optical imaging data as an input. Specific contributions from this work are as follows:

(1) We investigated the quality of thin-wall parts made using LPBF process as a function of their build orientation and aspect ratio (length-to-thickness ratio). The effect of aspect ratio and wall thickness was quantified by extracting statistical features from the offline X-ray computed tomography (XCT) scan images of thin-wall parts.

The number of layers (vertical height) of a thin-wall part that can be built without damage is contingent on its aspect ratio and build orientation. It is recommended that a thin-wall be built with 0° orientation angle with respect to the recoater blade direction. In other words, the broadside of the thin-wall should not, as far as possible, face the recoater blade direction.

Further, thin-walls with thickness less than 0.1 mm generally fail to build irrespective of their orientation, as they are too weak to resist the shear force exerted by the recoater.

(2) Four quantifiers were defined and extracted from XCT images to characterize the build quality of the thin-wall. These quantifiers were aggregated in terms of the Mahalanobis-squared distance.

(3) We trained a CNN to predict the thin-wall quality (in terms of the Mahalanobis-squared distance) based on in-situ optical images of the part. For the representative cases, the Pearson correlation coefficient (ρ) between the Mahalanobis-squared distances measured from the XCT scan signatures and CNN derived predictions was in the range of 85% to 98%.

This work thus makes an early foray into detecting the onset of build failures in AM parts based on in-situ imaging through a CNN. However, the following question remains to be addressed, which we will endeavor to answer in our future research in the area:

- What is the generalizability of the approach proposed to reduce variations in other types of structures for different part designs and process conditions (e.g., laser power and velocity)?
- What is the applicability of the CNN proposed in this work for other types of features and LPBF machines through transfer learning?

Acknowledgements

Funding at Pennsylvania State University.

The experimental portion of this work was supported by the Air Force Research Laboratory through America makes under Agreement No. FA8650-12-2-7230. This work is supported in part by the National Science Foundation (NSF) grant CMMI-1617148. We gratefully acknowledge the valuable contributions of the faculty, staff, and students at Penn State's Center for Innovative Materials Processing through Direct Digital Deposition (CIMP-3D) for providing the data utilized in this research.

Funding at University of Nebraska-Lincoln.

One of the authors (PKR) thanks the NSF for funding his work through the following grants CMMI-1719388, CMMI-1739696 and CMMI-1752069 (CAREER) at University of Nebraska-Lincoln. Specifically, this work was funded through CMMI-1752069 wherein the concept of using in-situ imaging and big data analytics techniques to detect and diagnose formation of defects was proposed.

References

[1] Sames, W. J., List, F. A., Pannala, S., Dehoff, R. R., and Babu, S. S., 2016, "The metallurgy and processing science of metal additive manufacturing," International Materials Reviews, 61(5), pp. 315-360.doi:10.1080/09506608.2015.1116649

[2] DebRoy, T., Wei, H., Zuback, J., Mukherjee, T., Elmer, J., Milewski, J., Beese, A., Wilson-Heid, A., De, A., and Zhang, W., 2018, "Additive manufacturing of metallic components–process, structure and properties," Progress in Materials Science, 92, pp. 112-224.doi:https://doi.org/10.1016/j.pmatsci.2017.10.001

[3] Yavari, M. R., Cole, K. D., and Rao, P., 2019, "Thermal Modeling in Metal Additive Manufacturing Using Graph Theory," Journal of Manufacturing Science and Engineering, 141(7), p. 071007

[4] Wang, Z., Palmer, T. A., and Beese, A. M., 2016, "Effect of processing parameters on microstructure and tensile properties of austenitic stainless steel 304L made by directed energy deposition additive manufacturing," Acta Materialia, 110, pp. 226-235

[5] Imani, F., Gaikwad, A., Montazeri, M., Rao, P., Yang, H., and Reutzel, E., 2018, "Process Mapping and In-Process Monitoring of Porosity in Laser Powder Bed Fusion Using Layerwise Optical Imaging," Journal of Manufacturing Science and Engineering, 140(10), pp. 101009-101009-101014.doi:10.1115/1.4040615

[6] Mazur, M., Leary, M., Sun, S., Vcelka, M., Shidid, D., and Brandt, M., 2016, "Deformation and failure behaviour of Ti-6Al-4V lattice structures manufactured by selective laser melting (SLM)," The International Journal of Advanced Manufacturing Technology, 84(5), pp. 1391-1411.doi:10.1007/s00170-015-7655-4

[7] Frazier, W. E., 2014, "Metal Additive Manufacturing: A Review," Journal of Materials Engineering and Performance, 23(6), pp. 1917-1928.doi:10.1007/s11665-014-0958-z

[8] Zwier, M. P., and Wits, W. W., 2016, "Design for additive manufacturing: Automated build orientation selection and optimization," Procedia CIRP, 55, pp. 128-133.doi:https://doi.org/10.1016/j.procir.2016.08.040.

[9] Gao, W., Zhang, Y., Ramanujan, D., Ramani, K., Chen, Y., Williams, C. B., Wang, C. C., Shin, Y. C., Zhang, S., and Zavattieri, P. D., 2015, "The status, challenges, and future of additive manufacturing in engineering," Computer-Aided Design, 69, pp. 65-89.doi:https://doi.org/10.1016/j.cad.2015.04.001

[10] Gaikwad, A., 2019, "On Geometric Design Rules and In-process Build Quality Monitoring of Thin-Wall Features made using Laser Powder Bed Fusion Additive Manufacturing Process," Master of Science, University of Nebraska-Lincoln.

[11] Dunbar, A., Denlinger, E., Heigel, J., Michaleris, P., Guerrier, P., Martukanitz, R., and Simpson, T., 2016, "Development of experimental method for in situ distortion and temperature measurements during the laser powder bed fusion additive manufacturing process," Additive Manufacturing, 12, pp. 25-30.doi:https://doi.org/10.1016/j.addma.2016.04.007

[12] Dunbar, A. J., Denlinger, E. R., Gouge, M. F., Simpson, T. W., and Michaleris, P., 2017, "Comparisons of laser powder bed fusion additive manufacturing builds through experimental in situ distortion and temperature measurements," Additive Manufacturing, 15, pp. 57-65.doi:https://doi.org/10.1016/j.addma.2017.03.003

[13] Jacobsmühlen, J. z., Kleszczynski, S., Witt, G., and Merhof, D., 2015, "Detection of elevated regions in surface images from laser beam melting processes," IECON 2015 - 41st Annual Conference of the IEEE Industrial Electronics Society, pp. 001270-001275doi:10.1109/IECON.2015.7392275.

[14] Grasso, M., and Colosimo, B. M., 2017, "Process defects and in situ monitoring methods in metal powder bed fusion: a review," Measurement Science and Technology, 28(4), p. 044005.doi:https://doi.org/10.1088/1361-6501/aa5c4f

[15] Spears, T. G., and Gold, S. A., 2016, "In-process sensing in selective laser melting (SLM) additive manufacturing," Integrating Materials and Manufacturing Innovation, 5(1), p. 2.doi:10.1186/s40192-016-0045-4

[16] Gong, H., 2013, "Generation and detection of defects in metallic parts fabricated by selective laser melting and electron beam melting and their effects on mechanical properties," Ph.D., University of Lousville.

[17] Mani, M., Lane, B., Donmez, A., Feng, S., Moylan, S., and Fesperman, R., 2015, "NISTIR 8036: Measurement Science Needs for Real-time Control of Additive Manufacturing Powder Bed Fusion Processes," NIST, Gaithersburg, MD.

[18] Everton, S. K., Hirsch, M., Stravroulakis, P., Leach, R. K., and Clare, A. T., 2016, "Review of in-situ process monitoring and in-situ metrology for metal additive manufacturing," Materials & Design, 95, pp. 431-445.doi:https://doi.org/10.1016/j.matdes.2016.01.099

[19] Yao, B., Imani, F., Sakpal, A. S., Reutzel, E. W., and Yang, H., 2018, "Multifractal analysis of image profiles for the characterization and detection of defects in additive manufacturing," Journal of Manufacturing Science and Engineering, 140(3), p. 031014

[20] Huang, Y., Leu, M. C., Mazumder, J., and Donmez, A., 2015, "Additive Manufacturing: Current State, Future Potential, Gaps and Needs, and Recommendations," Journal of Manufacturing Science and Engineering, 137(1), pp. 014001-014001-014010.doi:10.1115/1.4028725

[21] Gobert, C., Reutzel, E. W., Petrich, J., Nassar, A. R., and Phoha, S., 2018, "Application of supervised machine learning for defect detection during metallic powder bed fusion additive manufacturing using high resolution imaging," Additive Manufacturing, 21, pp. 517-528.doi:https://doi.org/10.1016/j.addma.2018.04.005

[22] Abdelrahman, M., Reutzel, E. W., Nassar, A. R., and Starr, T. L., 2017, "Flaw detection in powder bed fusion using optical imaging," Additive Manufacturing, 15, pp. 1-11.doi:https://doi.org/10.1016/j.addma.2017.02.001

[23] Scime, L., and Beuth, J., 2018, "Anomaly detection and classification in a laser powder bed additive manufacturing process using a trained computer vision algorithm," Additive Manufacturing, 19, pp. 114-126.doi:https://doi.org/10.1016/j.addma.2017.11.009

[24] Scime, L., and Beuth, J., 2018, "A multi-scale convolutional neural network for autonomous anomaly detection and classification in a laser powder bed fusion additive manufacturing process," Additive Manufacturing, 24, pp. 273-286

[25] Yuan, B., Guss, G. M., Wilson, A. C., Hau-Riege, S. P., DePond, P. J., McMains, S., Matthews, M. J., and Giera, B., 2018, "Machine-Learning-Based Monitoring of Laser Powder Bed Fusion," Advanced Materials Technologies, 3(12), p. 1800136.doi:10.1002/admt.201800136

[26] Williams, J., Dryburgh, P., Clare, A., Rao, P., and Samal, A., 2018, "Defect Detection and Monitoring in Metal Additive Manufactured Parts through Deep Learning of Spatially Resolved Acoustic Spectroscopy Signals," Smart and Sustainable Manufacturing Systems, 2(1), pp. 204-226.doi:10.1520/SSMS20180035

[27] Aminzadeh, M., 2016, "A machine vision system for in-situ quality inspection in metal powder-bed additive manufacturing," Georgia Institute of Technology.

[28] Clijsters, S., Craeghs, T., Buls, S., Kempen, K., and Kruth, J.-P., 2014, "In situ quality control of the selective laser melting process using a high-speed, real-time melt pool monitoring system," The International Journal of Advanced Manufacturing Technology, 75(5-8), pp. 1089-1101

[29] Chen, R., Imani, F., Reutzel, E., and Yang, H., 2018, "From Design Complexity to Build Quality in Additive Manufacturing—A Sensor-Based Perspective," IEEE sensors letters, 3(1), pp. 1-4

[30] Imani, F., Chen, R., Diewald, E., Reutzel, E., and Yang, H., 2019, "Deep Learning of Variant Geometry in Layerwise Imaging Profiles for Additive Manufacturing Quality Control," Journal of Manufacturing Science and Engineering, 141(11)

[31] Thomas, D., 2009, "The development of design rules for selective laser melting," Ph.D. Dissertation, University of Wales.

[32] Kranz, J., Herzog, D., and Emmelmann, C., 2015, "Design guidelines for laser additive manufacturing of lightweight structures in TiAl6V4," Journal of Laser Applications, 27(S1), p. S14001.doi:https://doi.org/10.2351/1.4885235

[33] Dunbar, A. J., Gunderman, G. J., Mader, M. C., and Reutzel, E. W., 2017, "Fabrication and Quality Assessment of Thin Fins Built Using Metal Powder Bed Fusion Additve Manufacturing," Solid Freeform Fabrication Symposium - An Additve Manufacturing ConferenceAustin, Texas, USA, p. 2650.

[34] Hagan, M. T., Demuth, H. B., and Beale, M., 1997, Neural Network Design, PWS Publishing, Boston, MA.

[35] LeCun, Y., and Bengio, Y., 2010, "Convolutional networks for images, speech, and time series," Proceedings of 2010 IEEE International Symposium on Circuits and Systems, pp. 253-256.

[36] Ioffe, S., and Sezegdy, C., 2015, "Batch Normalization: Accelerating Deep Network Training by Reducing Internal Covariate Shift," Computing Research Repository (CoRR).doi:arXiv:1502.03167

[37] Glorot, X., Bordes, A., and Bengio, Y., 2011, "Deep Sparse Rectifier Neural Networks," Proceedings of the Fourteenth International Conference on Artificial Intelligence and Statistics, G. Geoffrey, D. David, and D. Miroslav, eds., PMLR, Proceedings of Machine Learning Research, pp. 315--323.

[38] Bottou, L., 1991, "Stochastic gradient learning in neural networks," Proceedings of Neuro-Nımes, 91(8), p. 12

[39] LeCun, Y., Kavukcuoglu, K., and Farabet, C., 2010, "Convolutional networks and applications in vision," Proceedings of 2010 IEEE International Symposium on Circuits and Systems, pp. 253-256doi:10.1109/ISCAS.2010.5537907.

Appendix I

Nomenclature and abbreviations used in this work.

AM	Additive manufacturing
LPBF	Laser powder bed fusion
XCT	X-ray computed tomography
CNN	Convolutional neural network
CAD	Computer-aided design
DSLR	Digital single-lens reflex
l/t	Aspect ratio: length to thickness ratio
θ	Orientation angle of thin-walls
R^2	R-squared value: goodness-of-fit statistic
$\bar{t}$	Thickness of thin-wall extracted from XCT images
ρ_t	Density of thin-wall extracted from XCT images
σ_s	Smoothness of thin-wall edge extracted from XCT images
δ	Degree of discontinuity in thin-wall extracted from XCT images
X^{θ}	Quantifier matrix
$(D_M^2)_i^{\theta}$	Mahalanobis-squared distance
$\bar{X}_i^{\theta}$	Vector containing features extracted from XCT images
μ^{TW}	Vector containing features extracted from CAD images
S^{-1}	Inverse of the variance-covariance matrix
$\overline{t_{CAD}}$	Thickness of thin-wall extracted from CAD images
$\sigma_{S(CAD)}$	Smoothness of thin-wall edge extracted from CAD images
$\rho_{t(CAD)}$	Density of thin-wall extracted from CAD images
$\delta_{(CAD)}$	Degree of discontinuity in thin-wall extracted from CAD images

Appendix II

This section details the approach adopted to detect build failure in thin-walls by two-phase analysis of the in-process powder bed images: (1) the extraction of individual images of the thin-wall from the noisy powder bed images, and (2) predicting the quality of these images as inputs to a convolutional neural network (CNN) which is trained to predict the build quality of the thin-wall. We used an image filtering technique to sharpen the image and negate the noisy background as depicted in Figure 14. The resulting binary image has clearly demarcated edges for each of the thin-walls. This step is done with the help of linear filtering operation which is termed as convolution filter (not be confused with a CNN). Convolution is an operation in which the output pixel is the weighted sum of a set of neighborhood input pixels. The matrix of weights is called the convolution kernel, also known as the filter. Figure 14 shows the convolution kernel used in this case where x is a variable which controls the intensity of sharpening of the image i.e. higher the value of x, the higher the erosion of the image.

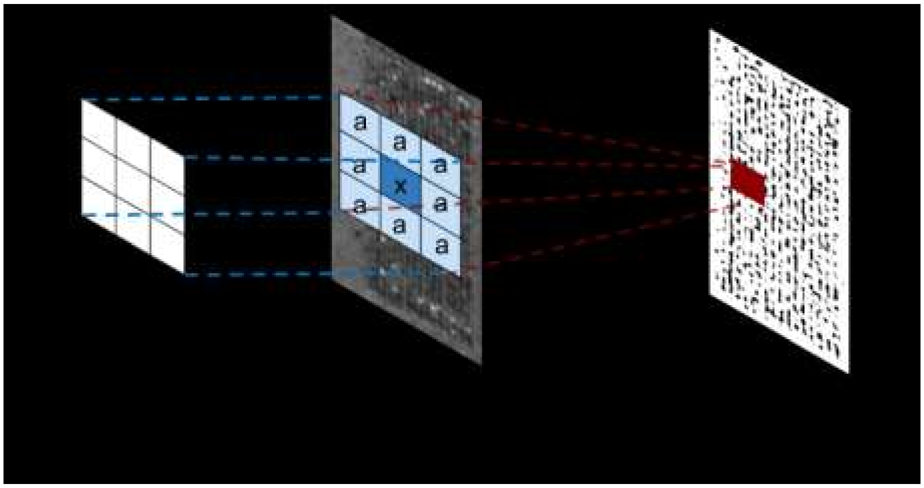

Figure 14: A schematic representation of image de-noising done by employing image sharpening. This technique uses a filter matrix which convolves around an image.

Convolutional neural network architecture

This section will briefly contrast the concept of the convolutional neural networks (CNN), vis-à-vis conventional feed-forward artificial neural networks (ANN) before providing mathematical details. ANNs are neurophysiologically inspired algorithms with neurons as their elementary units [34]. These neurons receive multiple inputs from either the input data or other neurons, later of the two being recurrent, and subsequently create an output by employing a non-linear transformation. The learning process to obtain the weights of the neurons is carried out using an algorithmic approach [26]. In a feed-forward ANN, neurons in a layer are fully connected, i.e., a neuron will be connected to all the neurons in the preceding and succeeding layer, and are independent of each other. Due to this reason, ANNs are computationally expensive to implement back-propagation when analyzing high volume of data, and further, ANNs do not encapsulate the spatiotemporal correlation within the data, such as images.

The CNN used in this work has four blocks along with a fully-connected layer, regression layer, input and output layer as seen in Figure 15. The input to the network is a binarized optical image of a single thin-wall in the size of 28 × 28 pixels which is extracted from de-noised layer-wise powder bed image, and the output is the corresponding Mahalanobis-squared distance of the thin-wall at the given layer. Each block has a 2D convolution layer with a rectified linear unit (ReLU), a batch normalization layer, and an average pooling layer.

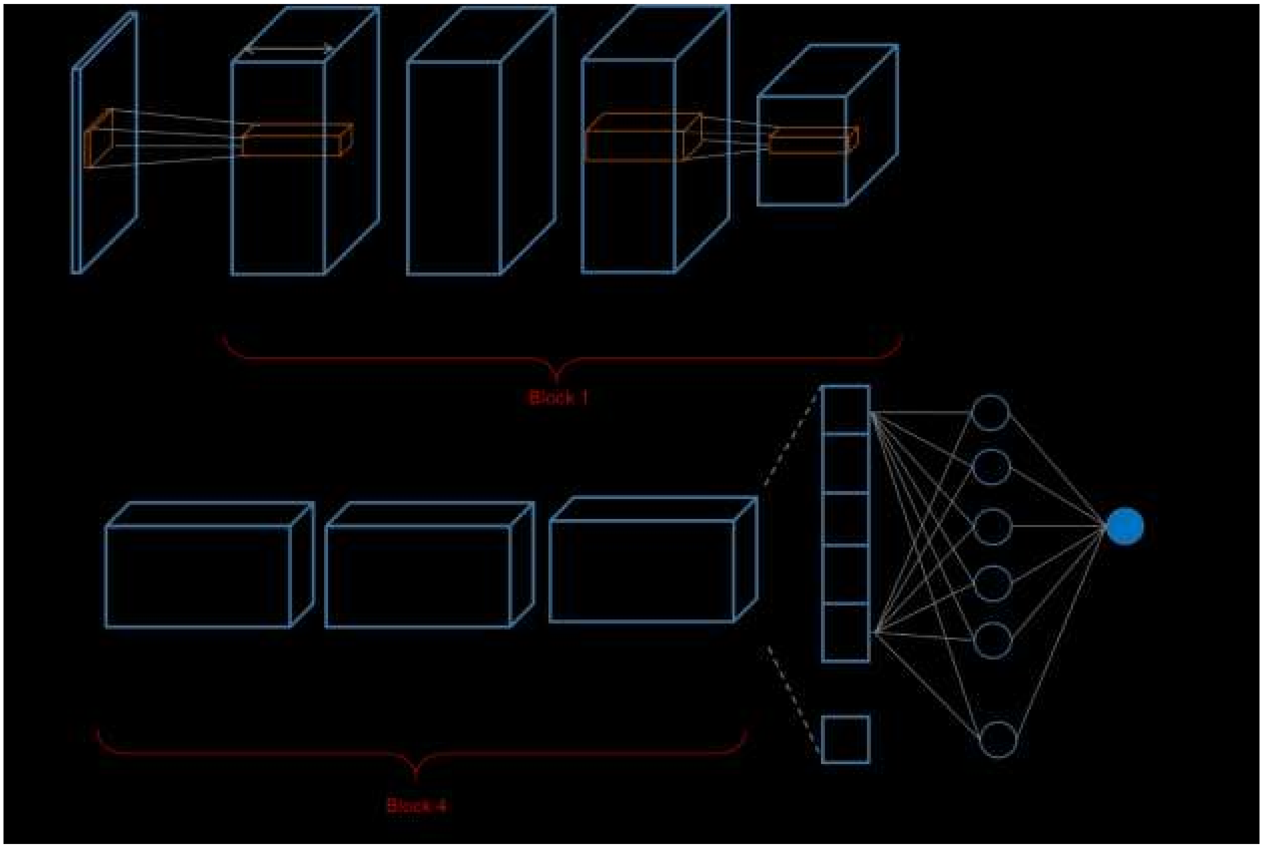

Figure 15: A schematic representation of the convolutional neural network architecture.

Convolutional layer

The convolutional layer extracts features from an image by learning various convolving filters [35]. In this CNN architecture, we use an increasing number of filters in each convolutional layers to extract complex features from the images. A filter is a $f \times f$ matrix, which convolves around an image and creates a feature map by performing a dot product operation on the input image, as shown in Figure 17. The manner in which the filter convolves over the input image is determined by a hyper-parameter called *stride*. Figure 17 (b1), is an illustration of a filter sliding over an image with stride set to 1. To preserve the dimensions of the images being convolved, the images are padded with zeros, i.e. the images are surrounded by zeros, before the convolution operation, and this hyper-parameter is called *padding*.

The convolutional neural network used in this work has four blocks, and each block has a convolutional layer in it, as shown in Figure 16. As the network gets deeper, the number of filters in each convolutional layer increases to extract high-level features from the image. This is represented in Figure 15 that the input image has a depth of 1 as it is a grayscale image, but the first convolution layer has a depth of 8 filters. The depth of a layer is a function of the number of filters employed in a convolution layer, and the last convolution layer in block 4 has a depth of 32 filters.

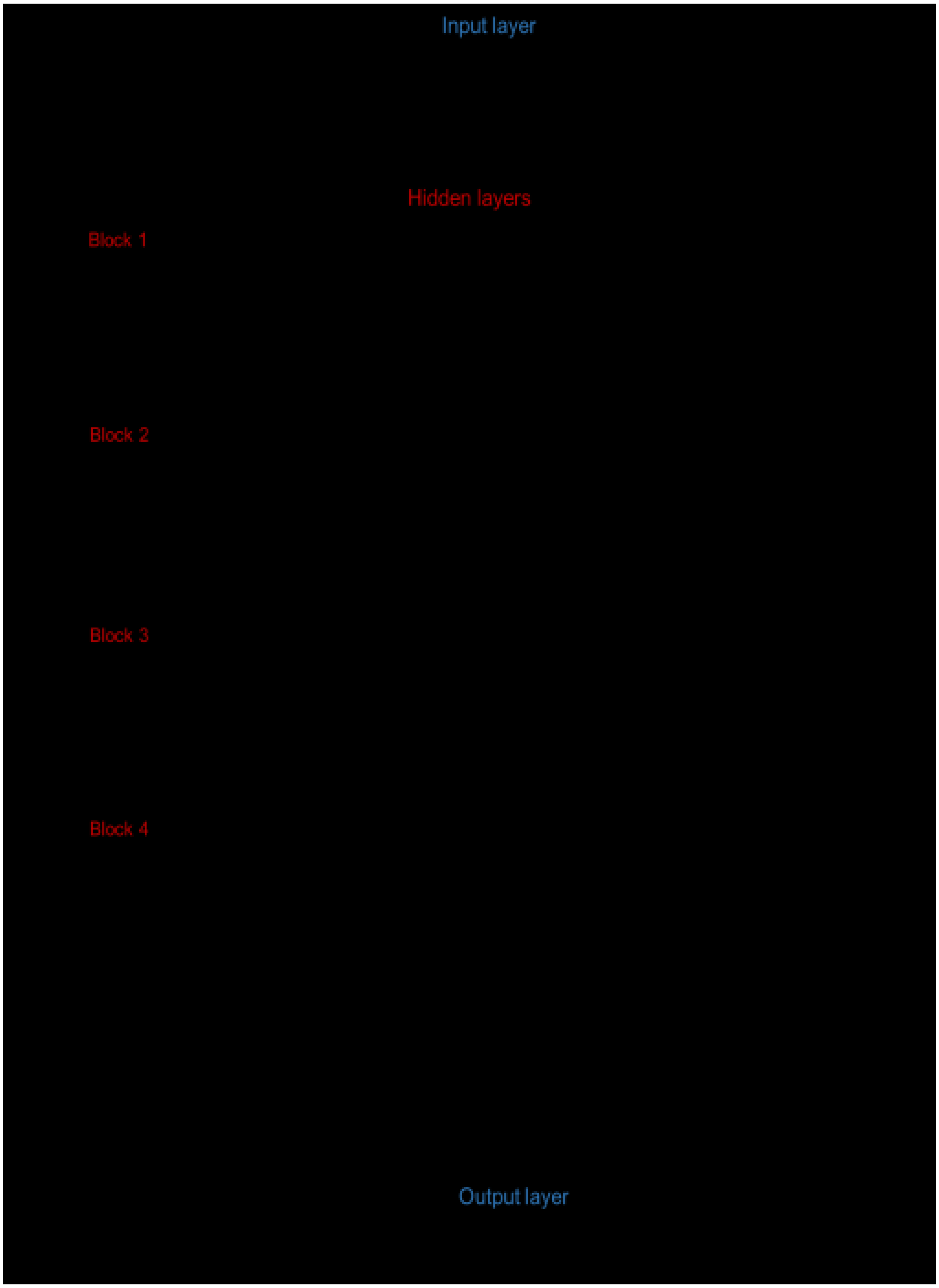

Figure 16: Flow-chart of the architecture of the convolutional neural network employed in this work to predict Mahalanobis-squared distance.

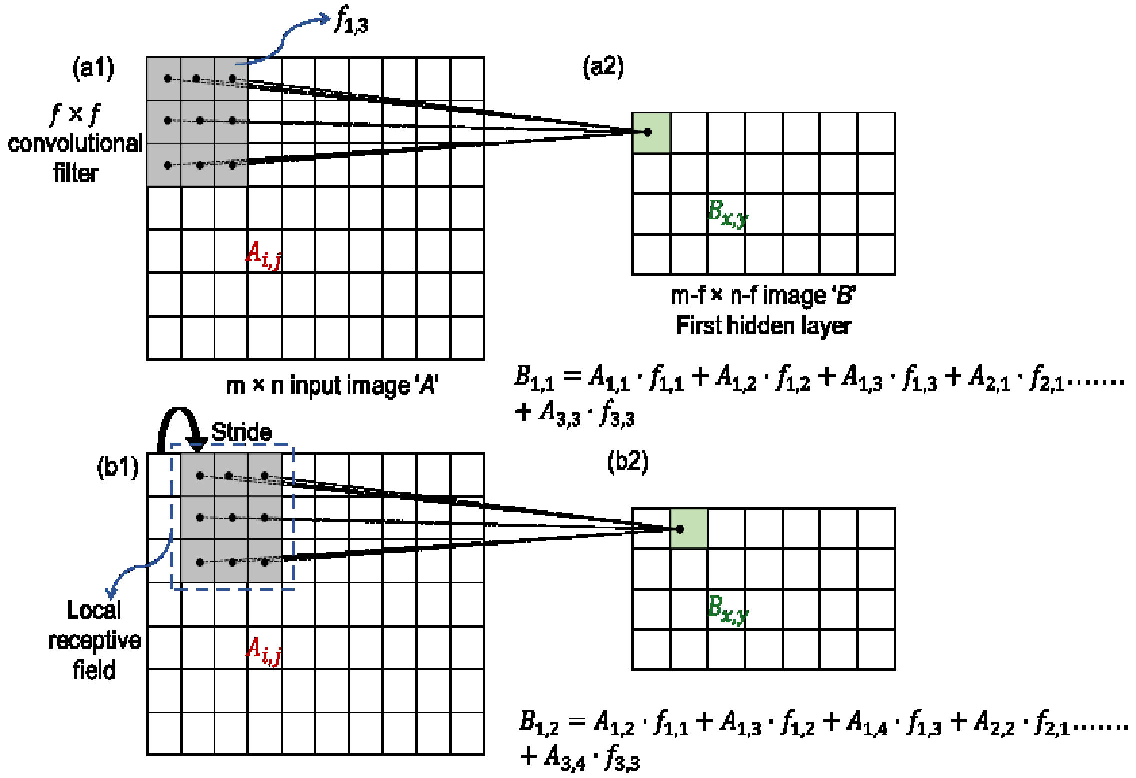

Figure 17: Schematic representation of convolution operation.

Batch normalization layer

The input given to a neural network is normalized, i.e. it has zero mean and unit variance, and this is done to quicken the learning process of the network. When the input variables of a network have extremely varying ranges, for example, one variable has a range of 1-1000, whereas the second one has a range of 1-2, the network parameters will have correspondingly wide range. This leads to a wide cost function in the direction of the variable with a wide range as it contributes more towards learning of the network. Due to this imbalance in the variables and the resulting elongated cost function, it becomes cumbersome to train a network. On the contrary, a neural network with normalized inputs has a circular cost function resulting in increased ease and speed of training. Likewise, it is advisable in deep neural network to normalize the input to every layer of the network, with the help of a technique called batch normalization [36].

When updating weights in one layer in a deep neural network, it is assumed that the layer's inputs will remain constant. However, the distribution of the input might change every time we update the weights, as the previous layer parameters are updated as well. In deep models, even small changes in earlier layers amplify drastically in the later layer, which significantly changes the input distribution to the later layers as well, making it hard for them to adapt to the changes, and thus, hindering convergence. This phenomenon is referred to as internal covariate shift, and batch normalization layers are employed in a deep neural network to prevent this phenomenon.

In batch normalization, the inputs are firstly normalized to zero mean and unit variance as shown below in Eqn. (3)-(5). This normalization is not performed on the whole input population at once, but is done on the input in batches [36].

$$\mu_B = \frac{1}{n}\sum_{k=1}^{n} a_k \tag{3}$$

$$\sigma_B{}^2 = \frac{1}{n}\sum_{k=1}^{n} (a_k - \mu_B)^2 \tag{4}$$

$$\widehat{a_k} = \frac{a_k - \mu_B}{\sqrt{\sigma_B{}^2}} \tag{5}$$

where, μ_B and $\sigma_B{}^2$ are the mean and variance of the batch respectively. $\widehat{a_k}$ is the normalized input value, and n is the batch size. Subsequently, the normalized inputs ($\widehat{a_k}$) are scaled and shifted to have an arbitrary mean and variance of the input distribution (Eqn. (6)).

$$o_k = \delta \widehat{a_k} + \alpha \tag{6}$$

where, o_k is an output of the batch normalization layer, and accordingly is the input to the activation (ReLU) layer. δ is the scaling factor, and α is the shifting factor, and these factors facilitate in randomizing the mean and variance of the batch inputs. Intuitively, it can be argued that these factors nullify the effect of normalization, as prior batch normalization, the data had random mean and variance. Taking a step backward, we can see that the mean and variance without batch normalization are dependent on excessively high number of parameter, such as, weights and biases of each neuron, activations etc., but in case of batch normalization they are dependent only on the two scaling and shifting factors which are trainable and learnable by the network.

When testing the network, the μ_B and ${\sigma_B}^2$ are not available, so the estimated of the population expectation and population variance are calculated as follows.

$$E_{k+1}[x] = \delta E_k[x] + (1-\alpha)\, \mu_B \tag{7}$$

$$Var_{k+1}[x] = \delta Var_k[x] + (1-\alpha)\, {\sigma_B}^2 \tag{8}$$

In our neural network architecture used in this work, a batch normalization layer is employed as shown in Figure 16.

Rectified linear unit (ReLU) layer

The rectified linear unit (ReLU) is an activation function (non-linearity) which sets all negative values to zero [37]. It is formally given as follows.

$$f(x) = \begin{cases} x & if\ x \geq 0 \\ 0 & if\ x < 0 \end{cases} \tag{9}$$

The ReLU layers are preferred over other activation functions, such as the sigmoid function and the hyperbolic tangent (tanh) function, because it is found that the ReLU layers significantly accelerate the convergence of the stochastic gradient descent, i.e., the ability of the network to reach its cost/loss function minima [38]. Further, the ReLU layers are computationally inexpensive as they only involve thresholding of an activation matrix, whereas the sigmoid and tanh functions need heavy computations. Also, the ReLU layers avoid vanishing of the gradient which is quite evident in the hyperbolic tangent function and sigmoid. Neural networks that are trained with the help of gradient-based learning method and backpropagation method often encounter the vanishing-gradient problem [37].

These methods, provide the neurons with updated weights that are proportional to the partial derivative of the error function (the difference between the value predicted by the network and the actual value) with respect to the current weights of the neurons in each training iteration. When activation functions such as the tanh function and sigmoid function are used, the vanishing gradient problem is observed, as they have gradients in the range (0, 1), and backpropagation computes gradients by the chain rule. This results in the multiplication of n of these small numbers to compute gradients of the initial layers in a n -layer network, meaning that the gradient (error signal) decreases exponentially with n while the initial layers train very slowly. In other words, vanishingly small gradients prevent the training of the network as the weights remain constant after every iteration. In our network, we have used the ReLU layer in each block after the batch normalization layer as seen in Figure 15 & Figure 16.

Average pooling layer

The average pooling layers are used to down-sample the spatial arrangement of an image (Figure 15) to reduce the computation, and also to avoid over-fitting, i.e., the network gets highly fitted to the training data, and cannot adapt to the inputs of the testing data, thus performing poorly. The spatial reduction is performed as it is sufficient to know the relative position of features with respect to other features, rather than knowing the exact feature location. Similar to a convolution layer, in an average pooling layer, filters of a given size move around an image in a non-overlapping manner, resulting in a single value which is the average of all values of the image in the given filter size (Figure 18) [39]. Along with filter size, another hyper-parameter that the average pooling layer employs is stride, which dictates the movement of the filter over the image. The layer individually operates on each of the depth slice of the input image, thus conserving that dimension (Figure 15), and also the feature data accumulated from various filters.

In this work, we use average pooling layers in the first two blocks as seen in Figure 16. This layer is not used in the succeeding layers to avoid significant reduction in the spatial dimensions of the image resulting in feature data loss. The pooling layers use a filter size of 2×2, and a stride of 2 in both blocks (Figure 18). This results in the reduction of input image size from 28×28, to 7×7 at the end of the second block.

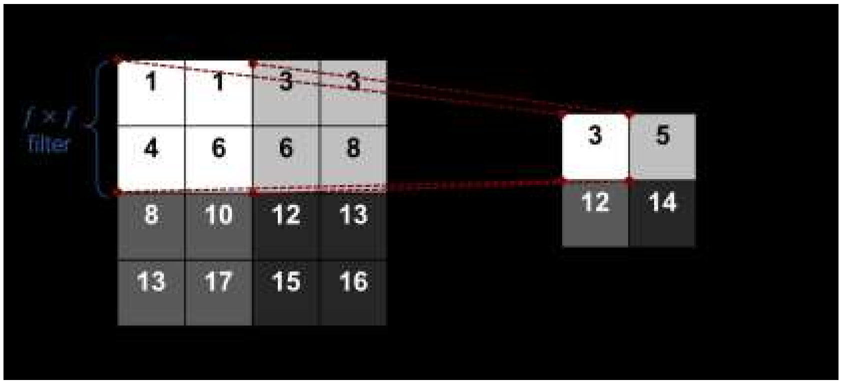

Figure 18: Schematic representation of an average pooling operation.

Fully connected layer

In a fully connected layer, all the neurons in the adjacent layers are pairwise connected to each other, but neurons in the same layers are independent of each other. Unlike a convolutional layer, the fully connected layer is a one-dimensional vector which has all activations of the previous layer, as seen in Figure 15. Due to this drastic change in dimension, fully–connected layers are placed at the end of the network, and convolution layers cannot be placed after them. Each convolution layer identifies features (e.g., lines, edges, curves, shapes) with the help of various filters, the fully-connected layer fuses these features together and come up with a prediction close to the desired output. The fully-connected layer in this network has 1568 inputs from the previous non-linearized (ReLU) convolution layer, and has a single output which is passed to the regression layer.

The mean-squared-error (MSE) is calculated between the predicted output and the desired output. In this regression layer, based on this MSE, weights of all neurons in the network are updated to obtain the optimum minima of the MSE. For training the network, values of hyperparameters like maximum epochs (maximum number of iterations), and the learning rate for weights, were heuristically set to achieve the lowest value of MSE. The value of maximum epochs was chosen in such a way that it avoided under the network training, and also avoided over-fitting. Similarly, the learning rate of weights, which is a hyper-parameter that controls the adjustment of the weights with respect to the cost function gradient, is set to an optimum level so as to preserve the network speed, and also not to miss out on a local minimum of the cost function.